

# Engineering of Single Magnetic Particle Carrier for living Brain cell imaging: A Tunable $T_1$ -/ $T_2$ -/Dual-Modal Contrast Agent for Magnetic Resonance Imaging application (MRI)

Yung-Kang Peng,<sup>†,‡</sup> Cathy N. P. Lui,<sup>‡,‡</sup> Yu-Wei Chen,<sup>§</sup> Shang-Wei Chou,<sup>§</sup> Elizabeth Raine,<sup>†</sup> Pi-Tai Chou,<sup>§</sup> Ken K.L. Yung<sup>‡,\*</sup> and S.C. Edman Tsang<sup>†,‡,\*</sup>

<sup>†</sup>Department of Chemistry, University of Oxford, Oxford OX1 3QR, UK

<sup>‡</sup>Department of Biology, Hong Kong Baptist University, Hong Kong

<sup>§</sup>Department of Chemistry, National Taiwan University, Taipei, Taiwan

<sup>#</sup>Applied Biology and Chemical Technology, Hong Kong Polytechnics University, Hong Kong

KEYWORDS: Magnetic resonance imaging • Dual-modal contrast agent • Magnetic field engineering • Safe magnetic manipulation

---

**ABSTRACT** Despite a variety of  $T_1$ - $T_2$  dual-modal contrast agents (DMCAs) reported for MRI, no tuning of local induced magnetic field strength of an DMCA which is important to modulate the overall  $T_1$  and  $T_2$  responses for imaging delicate cells, tissues and organs, is yet available. Here, we show that a spatial arrangement of  $T_1$  and  $T_2$  components within a ‘nano zone’ in a single core-shell nanoparticle carrier (i.e. DMCA with core  $\text{Fe}_3\text{O}_4$  and MnO clusters in a silica shell) to produce the necessary fine-tuning effect. It is demonstrated that this particle after the anti-CD133 antibody immobilization allows both  $T_1$  and  $T_2$  imaging at higher resolution for living ependymal brain cells of rodents with no local damage under a strong MRI magnetic field. This study opens a route to rational engineering of DMCAs for accurate magnetic manipulations in a safe manner.

---

## INTRODUCTION

$\text{Fe}_3\text{O}_4$ -based nanocomposites conjugated with recognition groups are commonly used for isolation, pre-concentration and separation of biological entities for a wide range of applications.<sup>[1,2]</sup> The superparamagnetic  $\text{Fe}_3\text{O}_4$  nanoparticles (NPs) also possess high magnetization which can cause field inhomogeneity perturbing the spin-spin relaxation of water protons, hence offering the  $T_2$  mode imaging for in-vivo MRI applications such as tumor cell tracking and early cancer diagnosis.<sup>[3,4]</sup> However, the induced long range magnetic field and the susceptibility artefacts distort the background image, which commonly mass off the fine detail required for clinical diagnosis in a typical negative (dark contrast)  $T_2$ -weighted MR image. In contrast,  $T_1$  contrast agents (CAs) comprise of paramagnetic species e.g. Gd (III) and Mn (II), which facilitate spin-lattice relaxation of only water protons in a close range. This is regarded as an advantageous alternative as they can provide positive (bright) MRI image at higher resolution.<sup>[5-8]</sup> However, the single mode contrast is not ideal and is increasingly facing challenges especially when accurately imaging small biological targets with different backgrounds. As a result, the use of  $T_1$ / $T_2$  dual contrast

agents is adopted by combining  $T_1$  and  $T_2$  contrast materials<sup>[9-15]</sup> or single component-based  $T_1$ - $T_2$  contrast agent.<sup>[16,17]</sup> In our early work,<sup>[18]</sup> we demonstrated  $\text{Fe}_3\text{O}_4$  NPs conjugated with CD133 antibody, which can extract cells with CD133 positive ( $\text{CD133}^+$ ) neural stem cells (NSCs) properties from the ependymal layers lining the ventricular-subventricular zone (V-SVZ) in rodent brain by using external magnetic separation. In addition, the distribution of these tagged NSC cells in living brain issue can be for the *first time* imaged by  $T_2$ -weighted MRI.<sup>[19]</sup> This may allow harvest of delicate cells, engineering and re-implantation in the future. However, as a typical  $T_2$ -weighted MRI CA, a severe damage to the host V-SVZ was found after the MRI scan presumably due to the field generated by MRI (4.7-Tesla used here) (vide infra), which was strong compared to the commercial in vitro cell separator (e.g. MiniMACS) with field strength usually < 0.5 T which shows no observable damage. This result rises concern about the safety use of those recognition group conjugated  $\text{Fe}_3\text{O}_4$ -based nanocomposites under strong external magnetic fields especially for in-vivo MRI in delicate tissues or organs such as the brain.

To reduce the intrinsic magnetization of  $\text{Fe}_3\text{O}_4$ -based nanocomposites and at the same time achieve a more

preferred dual  $T_1$ -/ $T_2$ - MR imaging, studies regarding to the incorporation of either antiferromagnetic or paramagnetic  $T_1$  materials with different spatial arrangements in a single particle carrier have been summarized in SI.<sup>[9-14]</sup> However, the systematical understanding of spatial spin-spin interactions between  $T_1$  and  $T_2$  materials in a single particle carrier and its correlation to MR imaging is still very limited.

To study the spin-spin interaction between  $T_1$  and  $T_2$  materials, we herein strategically design and prepare a  $T_1$ - $T_2$  dual-modal contrast agent (DMCA) comprising a 8 nm  $\text{Fe}_3\text{O}_4$  core and a functionalized mesoporous silica shell ( $\text{Fe}_3\text{O}_4(8)@\text{MnO}/\text{mSiO}_2\text{-CD133}$ , where ultra-small MnO clusters are dispersed within mesopores), which hosts anti-CD133 antibody on its outermost surface. These antiferromagnetic MnO clusters with higher electron spins ( $d_5$  electron system) placed in a close proximity of the  $\text{Fe}_3\text{O}_4$  core within the “nano influence zone” are clearly demonstrated to be capable of modulating the resulting magnetization field strength of the particle. This enables the tuning of the local field to reduce host damage due to magnetic induced agitation by MRI and at the same time achieve dual modal MR imaging. In contrast, placing a MnO containing particle to a separate  $\text{Fe}_3\text{O}_4$  particle beyond the “nano influence zone” did not show such effect. The induced magnetic field by  $\text{Fe}_3\text{O}_4@\text{MnO}/\text{mSiO}_2$  can be further tuned by using different sized core  $\text{Fe}_3\text{O}_4$  NPs. Interestingly, apart from an expected quenching of the  $T_1$  signal when a larger  $\text{Fe}_3\text{O}_4$  core (17.5 nm) is used ( $\text{Fe}_3\text{O}_4(17.5)@\text{MnO}/\text{mSiO}_2$ ), an “inverted MR phenomenon” from  $T_2$  CA to  $T_1$  CA is observed when MnO clusters are placed in a close proximity of a smaller  $\text{Fe}_3\text{O}_4$  core (3.7 nm) ( $\text{Fe}_3\text{O}_4(3.7)@\text{MnO}/\text{mSiO}_2$ ). It should be noted that even though the  $\text{MnO}/\text{Fe}_3\text{O}_4$   $T_1$ - $T_2$  DMCA<sup>[12,14]</sup> or related kinds of DMCA<sup>s</sup><sup>[9-11,13]</sup> have been studied, no further report on tuning the local induced magnetic field strength of DMCA is available. As demonstrated in this study, such induced magnetic response of DMCA, if not engineered, could cause serious damage to host cells by external magnetic field generated from MRI.

## EXPERIMENTAL SECTION

**Synthesis of 50 nm Mesoporous Silica NPs ( $\text{mSiO}_2$ ).** 364 mg of cetyltrimethylammonium bromide (CTAB, 99%, Acros) was dissolved in 100 mL DI water (80 °C) under intensive stirring and light-sealed environment. After a clear solution was obtained, 0.83 mL of tetraethyl orthosilicate (TEOS, 98%, Acros) was added dropwise for 20 min. Immediately, 148 mg of  $\text{NH}_4\text{F}$  ( $\geq 98.0\%$ , Fluka) which was used as a catalyzer for accelerating the hydrolyzation and condensation of silicon sources was added. After 1 h, nanoparticles were collected by centrifugation (14500 rpm, 10 min) and washed with ethanol and deionized water three times.

**Synthesis of  $\text{MnO}/\text{mSiO}_2$  NPs.** The as-prepared  $\text{mSiO}_2$  nanoparticles (see above) were used as template for synthesis of ultrasmall MnO NPs.<sup>[20]</sup> Typically, 30 mg of  $\text{mSiO}_2$  NPs (30 mg), 660 mg of  $\text{MnCl}_2 \cdot 4\text{H}_2\text{O}$  (99%,

Aldrich) and 10 mL of triethylene glycol (99%, Sigma-Aldrich) were added to a 50 mL three-necked flask and the mixture was magnetically stirred. The reaction temperature was then raised to 200 °C and kept at that temperature for 6 h before cooling to room temperature. The solvent, unreacted coating ligand, unreacted  $\text{Mn}^{2+}$ , and  $\text{Cl}^-$  ions were removed from the reaction solution by centrifugation (14500 rpm, 10 min). The bottom product,  $\text{MnO}/\text{mSiO}_2$  NPs were washed with deionized water for three times.

**Synthesis of Hydrophobic  $\text{Fe}_3\text{O}_4$  NPs.** The iron precursor, iron-oleate complex, was firstly prepared by reacting metal chlorides and sodium oleate. Typically, 1.08 g of  $\text{FeCl}_3 \cdot 6\text{H}_2\text{O}$  (97%, Fluka) and 3.65 g of sodium oleate ( $\geq 99\%$ , Sigma) were dissolved in a mixture solvent composed of 8 mL ethanol, 6 mL distilled water and 14 mL hexane. The resulting solution was heated to 70 °C and reacted for two hours. When the reaction was completed, the upper organic layer containing the iron-oleate complex was washed three times with 3 mL distilled water in a separatory funnel. After washing, hexane was evaporated off, resulting in iron-oleate complex in a waxy solid form. For the preparation of 8 nm  $\text{Fe}_3\text{O}_4$  NPs, 20 mg of the iron-oleate complex synthesized as described above and 300  $\mu\text{L}$  of oleic acid (90%, Acros) were dissolved in 20 mL of 1-octadecene (technical grade, 90%, Acros) at room temperature. The reaction mixture was heated to 310 °C with a constant heating rate of 5 °C  $\text{min}^{-1}$ , and then kept at that temperature for 30 min. The solution was then cooled to room temperature. Ethanol (40 mL) was added to the mixture, and a black material was precipitated and separated *via* centrifugation (14500 rpm, 10 min). The product, 8 nm  $\text{Fe}_3\text{O}_4$  NPs, was washed with isopropanol/hexane several times and dried in oven. The 3.7 nm and 17.5 nm  $\text{Fe}_3\text{O}_4$  NPs were prepared by the same procedure but different amount of oleic acid was added (150  $\mu\text{L}$  for 3.7 nm; 600  $\mu\text{L}$  for 17.5 nm).

**Synthesis of  $\text{Fe}_3\text{O}_4(x)@\text{SiO}_2$  ( $x = 3.7, 8$  and  $17.5$ ) NPs.**  $\text{Fe}_3\text{O}_4@\text{SiO}_2$  nanocomposites were prepared from reverse micelles using a previously reported procedure.<sup>[6]</sup> The as-prepared  $\text{Fe}_3\text{O}_4$  NPs (see above) were used as seeds for growth of the  $\text{SiO}_2$  shell. Briefly,  $\text{Fe}_3\text{O}_4$  nanoparticles (2 mg) and 100  $\mu\text{L}$  of TEOS were added to a heterogeneous solution containing cyclohexane (24 mL), hexanol (4.8 mL), Triton X-100 (Acros) (6 mL), and deionized water (1 mL). After 6 h of stirring,  $\text{NH}_4\text{OH}$  (28-30 wt%, Fluka) (100 mL) was added to initiate the hydrolysis of TEOS. The reaction was allowed to continue for another 24 h with stirring at room temperature. The product,  $\text{Fe}_3\text{O}_4@\text{SiO}_2$ , was well dispersed in ethanol and was further purified by centrifugation (14500 rpm, 10 min).

**Synthesis of  $\text{Fe}_3\text{O}_4(x)@\text{MnO}/\text{mSiO}_2$  ( $x = 3.7, 8$  and  $17.5$ ) NPs.** For the coating of mesoporous silica shell on  $\text{Fe}_3\text{O}_4$  NP ( $\text{Fe}_3\text{O}_4@\text{mSiO}_2$ ), first of all, two milliliters of  $\text{Fe}_3\text{O}_4$  NP (10 mg/mL in chloroform) were mixed with 300 mg of CTAB and 20 mL of deionized water. The mixture was then stirred vigorously until the formation of the oil-in-water microemulsion appeared with a turbid brown solution. Then the chloroform solvent was boiled off from

the solution, resulting in a transparent brown  $\text{Fe}_3\text{O}_4/\text{CTAB}$  solution. This solution was added to a mixture of 29.5 mL of water and 0.5 mL of 0.8 M NaOH solution, and the mixture was heated. At approximately 60°C under stirring, 0.5 mL of TEOS and 3 mL of ethyl acetate were loaded to the reaction solution in sequence. The solution stayed stirred for another 6 h and the resulting product,  $\text{Fe}_3\text{O}_4@m\text{SiO}_2$ , was washed by ethanol/water several times and collected by centrifugation (14500 rpm, 10 min). For the loading of MnO NPs in the mesoporous shell of as-synthesized  $\text{Fe}_3\text{O}_4@m\text{SiO}_2$  ( $\text{Fe}_3\text{O}_4@m\text{MnO}/m\text{SiO}_2$ ), the same procedure was adopted as the loading of MnO NPs in  $m\text{SiO}_2$  (see synthesis of  $\text{MnO}/m\text{SiO}_2$ ).

**Removal of CTAB Template.** Template molecules (CTAB) of  $\text{MnO}/m\text{SiO}_2$  and  $\text{Fe}_3\text{O}_4@m\text{MnO}/m\text{SiO}_2$  were removed via a fast and efficient ion exchange method. The NPs are transferred to 50 mL of ethanol containing 0.3 g of  $\text{NH}_4\text{NO}_3$  ( $\geq 99.0\%$ , Aldrich) and kept at 60°C for 2 h. The extraction step was repeated twice. After 6 h of dialysis, the product (without CTAB) was prepared and ready for use.

**Amine Modification.** In order to immobilize CD133 antibody on silica outmost surface, amine modification was firstly carried out on  $\text{MnO}/m\text{SiO}_2$ ,  $\text{Fe}_3\text{O}_4@m\text{SiO}_2$  and  $\text{Fe}_3\text{O}_4@m\text{MnO}/m\text{SiO}_2$ . Briefly, 3-amino-propyltrimethoxysilane (95%, Acros) (10  $\mu\text{L}$ ) was added to a mixture of ethanol (30 mL), deionized water (6 mL),  $\text{NH}_4\text{OH}$  (300  $\mu\text{L}$ ), and as-prepared NPs (20 mg).<sup>[3,4]</sup> After 24 h, the sample was centrifuged and washed several times to remove the unreacted chemicals. The precipitate of particles (i.e.  $\text{MnO}/m\text{SiO}_2\text{-NH}_2$ ,  $\text{Fe}_3\text{O}_4@m\text{SiO}_2\text{-NH}_2$  and  $\text{Fe}_3\text{O}_4@m\text{MnO}/m\text{SiO}_2\text{-NH}_2$ ) was then collected by centrifugation (14500 rpm, 10 min) and redispersed in deionized water.

**CD133 Immobilization.** The anti-CD133 antibodies (Milteny Biotec) were covalently conjugated onto the amine-functionalized silica surface by N-(3-dimethylaminopropyl)-N'-ethylcarbodiimide hydrochloride (EDC, Aldrich)/N-hydroxysuccinimide (NHS, 98%, Acros) coupling chemistry.<sup>[18,19]</sup> Typically, amine-functionalized particles (i.e.  $\text{MnO}/m\text{SiO}_2\text{-NH}_2$ ,  $\text{Fe}_3\text{O}_4@m\text{SiO}_2\text{-NH}_2$  and  $\text{Fe}_3\text{O}_4@m\text{MnO}/m\text{SiO}_2\text{-NH}_2$ ) (16 mg) were incubated with 10 mg EDC and 10 mg NHS for 30 min. Then, anti-CD133 antibodies (1 mL) were added to the mixture and incubated for 1 h at room temperature. The antibodies-conjugated nanocomposites ( $\text{MnO}/m\text{SiO}_2\text{-CD133}$ ,  $\text{Fe}_3\text{O}_4@m\text{SiO}_2\text{-CD133}$  and  $\text{Fe}_3\text{O}_4@m\text{MnO}/m\text{SiO}_2\text{-CD133}$ ) were purified by centrifugation (14500 rpm, 10 min) and washed 3-4 times with PBS (pH 7.4).

**Relaxation Measurement.** The  $r_1$  and  $r_2$  relaxation times were measured by 4.7-Tesla Biospec 47/40 MR scanner;  $r_2$  relaxation times were determined using a Carr Purcell Meiboom Gill (CPMG) sequence, with a recycle time of 10 s, eight averages with phase cycling, and 180° pulse separation of 1 ms. Monoexponential fitting was performed to even echoes over a 250 ms acquisition

window. The  $r_1$  relaxation was estimated using inversion recovery techniques, with a recycle time of 10 s, four averages with phase cycling, and eight inversion times logarithmically spaced over the interval 0–2000 ms. Linear regression between  $r_1/r_2$  and iron/manganese concentration was performed using standard techniques.

**In Vivo MRI Experiments.** Adult Sprague-Dawley (SD) rats (8 weeks of age, male, body mass  $\sim 300$  g) were employed in the experiments. All the animals were fully anesthetized with 5% isoflurane at 1 L  $\text{min}^{-1}$  air flow and fitted with a custom designed head holder inside the magnet of a 4.7-Tesla Biospec 47/40 MR scanner. 1–1.5% isoflurane was maintained at 1 L  $\text{min}^{-1}$  air flow throughout the whole experiments. The MRI experiments were performed before and at different times after the injection of three different CAs ( $T_1$  CA,  $T_2$  CA, DMCA) at a dose of 0.19  $\text{mg}\cdot\text{kg}^{-1}$  with ( $T_1/T_2$ ) TR = 500/5000 ms, ( $T_1/T_2$ ) T<sub>Eff</sub> = 8/70 ms, FOV = 7 cm  $\times$  7 cm, slice thickness = 1.3 mm, and matrix size = 256  $\times$  128 (zero-padded to 256  $\times$  256) with six repetitions.

**Instruments.** The shapes and size distributions of NPs were measured with a JEOL JEM 1230 transmission electron microscope (TEM). High resolution (HRTEM) images were taken with a JEOL JEM 2100F microscope operated at 200 kV. Experiments of X-ray energy dispersive spectroscopy (EDS) were performed by using a GENESIS 2000 EDS detector connected to the HRTEM instrument. Magnetic measurements were performed by superconducting quantum interference device (SQUID) magnetometer (MPMS, Quantum Design). The specific surface area of the sample was calculated based on the Brunauer–Emmett–Teller (BET) equation at P/P<sub>0</sub> between 0.05 and 0.3.

## RESULTS AND DISCUSSION

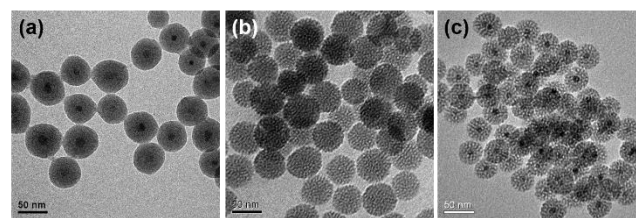


FIGURE 1. TEM images of (a)  $T_2$  CA ( $\text{Fe}_3\text{O}_4(8)@m\text{SiO}_2$ ), (b)  $T_1$  CA ( $\text{MnO}/m\text{SiO}_2$ ) and (c) DMCA ( $\text{Fe}_3\text{O}_4(8)@m\text{MnO}/m\text{SiO}_2$ ).  $\text{Fe}_3\text{O}_4(8)$ : 8 nm  $\text{Fe}_3\text{O}_4$ . See Figure S1b-d for corresponding low magnification TEM images

**Preparation and characterization of  $T_2$ ,  $T_1$  and DMCA contrast agents.** To comprehensively study the associated damage caused by DMCA ( $\text{Fe}_3\text{O}_4@m\text{MnO}/m\text{SiO}_2$ ), single modal  $T_2$  ( $\text{Fe}_3\text{O}_4@m\text{SiO}_2$ ) and  $T_1$  ( $\text{MnO}/m\text{SiO}_2$ ) contrast agents were also prepared for comparison. Scheme S1 summarizes the synthetic protocols of these three kinds of CA nanoparticles. The preparation of  $T_2$  ( $\text{Fe}_3\text{O}_4@m\text{SiO}_2$ ) is similar to our recent report.<sup>[6]</sup> For the preparation of nanoparticle-based  $T_1$  CA, we adopted a post-synthesis strategy that  $T_1$  CAs (MnO) can be homogeneously dispersed in the hydrophilic mesopo-

rous silica ( $\text{mSiO}_2$ ) framework as shown by Baek *et al.*<sup>[20]</sup> and our previous work.<sup>[21,22]</sup> Such a structural design not only makes MnO clusters inside the mesoporous  $\text{mSiO}_2$  channel free from surfactant coordination (increase parameter  $q$  of  $r_1^{15}$ ) but also provides mechanical resistance against clustering under physiological conditions.<sup>[8]</sup> More importantly, the average pore size of  $\text{mSiO}_2$  is  $\sim 2.5$  nm, which hosts the nano-clusters that can greatly increase the close contact of the MnO clusters with bound water molecules for local enhancement in  $T_1$  contrast.<sup>[8]</sup> Detailed design, preparation and characterization of  $T_2$  CA ( $\text{Fe}_3\text{O}_4(8)@SiO_2$ , 8 nm core  $\text{Fe}_3\text{O}_4$ , Figure 1a) and  $T_1$  CA ( $\text{MnO}/\text{mSiO}_2$ , Figure 1b) were elaborated in supporting information (Scheme S1 and Figure S1-6). The procedure to prepare DMCA particle ( $\text{Fe}_3\text{O}_4(8)@MnO/\text{mSiO}_2$ , 8 nm core  $\text{Fe}_3\text{O}_4$ ) is similar to  $T_1$  CA ( $\text{MnO}/\text{mSiO}_2$ ) but using  $\text{Fe}_3\text{O}_4(8)@mSiO_2$  instead of  $\text{mSiO}_2$  as template for the growth of MnO clusters (Scheme S1). Synthetic details of  $\text{Fe}_3\text{O}_4(8)@mSiO_2$  with shell thickness around 20 nm was elaborated in the experimental section. Briefly, hydrophobic 8 nm  $\text{Fe}_3\text{O}_4$  NPs (Figure S1a) were transferred to the aqueous phase by utilizing cetyltrimethylammonium bromide (CTAB). In the subsequent sol-gel reaction, CTAB-stabilized  $\text{Fe}_3\text{O}_4$  NPs act as seeds for the formation of spherical mesoporous silica shells by hydrolysis and condensation of TEOS. Herein, CTAB serves as not only the secondary stabilizer for the transfer of  $\text{Fe}_3\text{O}_4$  NPs to the aqueous phase but also the organic templates for the formation of the mesoporous silica shells. In this core/shell structure, the silica-CTAB layer is formed locally around the CTAB- $\text{Fe}_3\text{O}_4$  NPs under basic conditions through an electrostatic interaction between the cationic (CTAB) and anionic (silicate) species. The XRD, EDX and XPS analysis of the resulting product,  $\text{Fe}_3\text{O}_4(8)@MnO/\text{mSiO}_2$ , are shown in Figure S2, Figure S7 and Figure S8, respectively. As shown in TEM images of Figure 1c and Figure S1d, the final product, DMCA ( $\text{Fe}_3\text{O}_4(8)@MnO/\text{mSiO}_2$ ), with an average diameter around 45 nm are highly mono-dispersed (62.7 nm from DLS, Figure S9). The weight percent of  $\text{Fe}_3\text{O}_4$  and MnO in  $\text{Fe}_3\text{O}_4(8)@MnO/\text{mSiO}_2$  were calculated to be 37.9% and 26.3%, respectively. The corresponding relaxation properties of these  $T_2$  CA,  $T_1$  CA and DMCA are summarized in Table S1. As expected, the  $T_2$  CA particle ( $\text{Fe}_3\text{O}_4(8)@SiO_2$ ) shows the highest  $r_2/r_1$  ratio (94.94), while the  $T_1$  CA ( $\text{MnO}/\text{mSiO}_2$ ) particle shows the lowest  $r_2/r_1$  ratio of 10.17. The MR phantom imaging study (Figure S10) provides further evidence that both  $\text{Fe}_3\text{O}_4(8)@SiO_2$  and  $\text{MnO}/\text{mSiO}_2$  particles exhibit typical  $T_2$  and  $T_1$  CA characteristics, respectively. Only the  $\text{Fe}_3\text{O}_4(8)@MnO/\text{mSiO}_2$  particle, with  $r_2/r_1$  ratios in between (42.93, Table S1), shows MR signals in both  $T_1$ - and  $T_2$ -weighted imaging (Figure S10).

**MR field induced brain damage of tagged V-SVZ.** In order to immobilize the CD133 antibody on the outmost surface of the silica, amine modification was firstly carried out right after CTAB removal (Figure S11) and the CD133 antibodies can then be easily conjugated onto the amine-functionalized silica surface via coupling chemistry as

reported (see experimental section for details).<sup>[18,19]</sup> We unilaterally injected 5  $\mu\text{L}$  of  $T_1$  CA ( $\text{MnO}/\text{mSiO}_2\text{-CD133}$ ),  $T_2$  CA ( $\text{Fe}_3\text{O}_4(8)@SiO_2\text{-CD133}$ ) and DMCA ( $\text{Fe}_3\text{O}_4(8)@MnO/\text{mSiO}_2\text{-CD133}$ ) (2000  $\mu\text{g mL}^{-1}$  in PBS solution) into the left V-SVZ of rat brains, by a micro-syringe through a preformed hole on their skulls by micro-surgery (Figure S12), respectively to compare the MR contrast and damage to the tagged V-SVZ (NSCs host) under MR magnetic field of the traditional  $T_1/T_2$  CAs with our engineered DMCA particle.

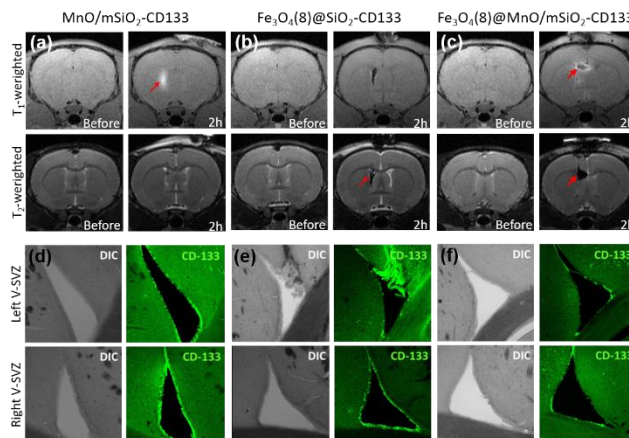


FIGURE 2. *In situ*  $T_1$ - $T_2$  MRI studies of (a)  $T_1$  CA ( $\text{MnO}/\text{mSiO}_2\text{-CD133}$ ), (b)  $T_2$  CA ( $\text{Fe}_3\text{O}_4(8)@SiO_2\text{-CD133}$ ) and (c) DMCA ( $\text{Fe}_3\text{O}_4(8)@MnO/\text{mSiO}_2\text{-CD133}$ ), were unilaterally injected into the left V-SVZ for the targeting of  $\text{CD133}^+$  NSCs (MR images were taken before and 2 hour after injection). (d)-(f) are corresponding optical images of left V-SVZ and right V-SVZ (no particle, control)

A positive (bright) contrast was noted in left V-SVZ of rat brains under the  $T_1$ -weighted MRI but not the  $T_2$ -weighted MRI with  $T_1$  CA (Figure 2a). As expected,  $T_2$  CA particle produced a dark image on MRI (Figure 2b). For DMCA, both  $T_1$ - and  $T_2$ - weighted images are achieved in the left V-SVZ of a living rat (Figure 2c). With the CD133 antibodies tagged CAs particles, all of them could specifically localize to  $\text{CD133}^+$  NSCs of V-SVZ linings and no dispersal of the particles could be observed in the brain fluid or other parts of the brain 2 hours after the injection. See Figure S13 for control experiment carried out for the particle without CD133 modification. To evaluate the damage to the host (V-SVZ) of tagged  $\text{CD133}^+$  NSCs induced by MR magnetic field, left and right (control) ventricle were surgically isolated after the MRI scan. As shown in Figure 2e, a typical damage on the left V-SVZ is evident when only  $T_2$  CA is used. On the contrary, no apparent damage to the left V-SVZ can be found with both  $T_1$  CA and DMCA detained with tagged stem cells (Figure 2d and 2f). This result clearly implies that the widely clinically-adopted iron-based  $T_2$  CAs for in-vivo imaging should be used with extra caution as they can cause serious damage to tagged host delicate tissue under the external magnetic field generated from MRI (not caused by the injection, see SI for details). If we attribute this uncontrolled tissue damage to the intrinsic difference in magnetic properties between  $\text{Fe}_3\text{O}_4$  (superparamagnetic) and MnO (antiferromagnetic) NP, the high magnetization of  $\text{Fe}_3\text{O}_4$  can

respond strongly and be agitated violently by MR magnetic field (cf. MnO), but some questions remain to be answered. First, why there is no observable damage to left V-SVZ using DMCA with the same sized core  $\text{Fe}_3\text{O}_4$  (8 nm) as  $T_2$  CA? Also, in addition to rendering DMCA with  $T_1$  imaging capacity, how does the incorporation of MnO clusters modify the induced magnetic field of  $\text{Fe}_3\text{O}_4$  under an external field?

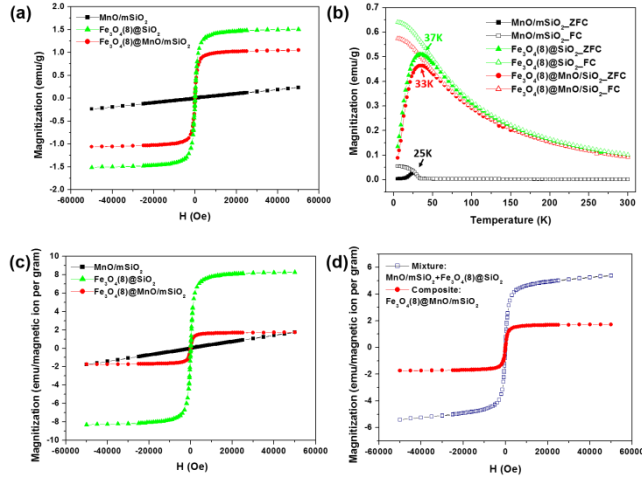
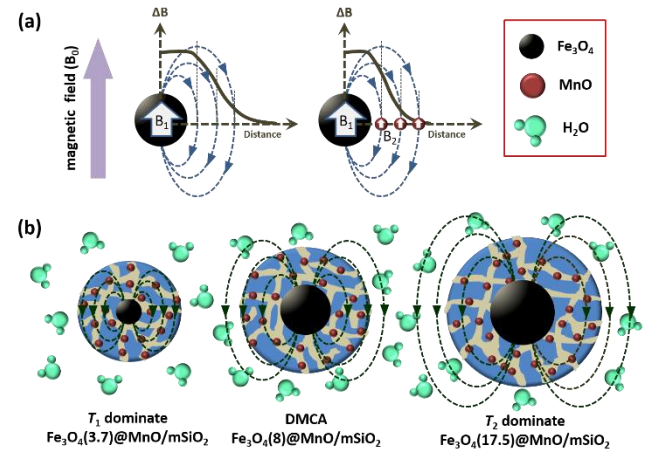


FIGURE 3. (a) Magnetization-hysteresis (M-H) and (b) magnetization-temperature (M-T) (both zero-field cooling (ZFC) and field cooling (FC)) curves of  $\text{MnO}/\text{mSiO}_2$ ,  $\text{Fe}_3\text{O}_4(8)@\text{SiO}_2$  and  $\text{Fe}_3\text{O}_4(8)@\text{MnO}/\text{mSiO}_2$ . (c) M-H curves of  $\text{MnO}/\text{mSiO}_2$ ,  $\text{Fe}_3\text{O}_4(8)@\text{SiO}_2$  and  $\text{Fe}_3\text{O}_4(8)@\text{MnO}/\text{mSiO}_2$  with magnetization normalized by per magnetic ion per gram. For  $\text{Fe}_3\text{O}_4(8)@\text{MnO}/\text{mSiO}_2$ , the magnetization was divided by  $[\text{Mn}]+[\text{Fe}]$ . (d) M-H curves of mixture:  $\text{MnO}/\text{mSiO}_2 + \text{Fe}_3\text{O}_4(8)@\text{SiO}_2$  and composite:  $\text{Fe}_3\text{O}_4(8)@\text{MnO}/\text{mSiO}_2$ . Both magnetization was divided by  $[\text{Mn}]+[\text{Fe}]$ .

**SQUID study of spin-spin interaction.** In order to investigate the spin-spin interaction between core  $\text{Fe}_3\text{O}_4$  and MnO clusters in the shell within the single nanoparticle, we then systematically studied the magnetic properties of  $\text{Fe}_3\text{O}_4(8)@\text{SiO}_2$ ,  $\text{MnO}/\text{mSiO}_2$  and  $\text{Fe}_3\text{O}_4(8)@\text{MnO}/\text{mSiO}_2$  particles invoking superconducting quantum interference device (SQUID). As shown in magnetization-hysteresis (M-H) measurement (Figure 3a), the magnetization of  $\text{MnO}/\text{mSiO}_2$  at room temperature increases proportionally to the external magnetic field whereas  $\text{Fe}_3\text{O}_4(8)@\text{SiO}_2$  quickly reaches saturation at below 10,000 Oe. This typical response of  $T_1$  and  $T_2$  CAs is due to the surface spin canting effect and the difference in the spin structure of MnO and  $\text{Fe}_3\text{O}_4$  NPs (see SI for details).<sup>[8]</sup> The single DMCA nanoparticle, as expected, reveals dual  $T_1$  and  $T_2$  properties in the M-H plot (Figure 3a) and possesses a mediate blocking temperature at 33 K (cf. 25 K for  $\text{MnO}/\text{mSiO}_2$  and 37 K for  $\text{Fe}_3\text{O}_4(8)@\text{SiO}_2$ ) (Figure 3b). The magnetization of M-H curve was further expressed per magnetic ion per gram. As shown in Figure 3c, the apparent high magnetization of  $\text{Fe}_3\text{O}_4(8)@\text{SiO}_2$  per magnetic ion per gram comparing to  $\text{MnO}/\text{mSiO}_2$  and  $\text{Fe}_3\text{O}_4(8)@\text{MnO}/\text{mSiO}_2$  is attributed to highly cooperative spin alignment within the super-paramagnetic iron oxide cores while the antiferromagnetic  $\text{MnO}/\text{mSiO}_2$  gives the

lowest magnetization. To visualize the distance-dependent interaction between spins of  $\text{Fe}_3\text{O}_4$  and MnO,  $\text{Fe}_3\text{O}_4(8)@\text{SiO}_2$  and  $\text{MnO}/\text{mSiO}_2$  were physically mixed with the same  $[\text{Fe}]/[\text{Mn}]$  ratio (1.34, Table S2) of their composite form,  $\text{Fe}_3\text{O}_4(8)@\text{MnO}/\text{mSiO}_2$  (Figure 3d). It should be noted that, in the physically mixed case, the silica spacer between the  $\text{Fe}_3\text{O}_4$  NP and the nearest MnO cluster in  $\text{MnO}/\text{mSiO}_2$  is considerably larger than that reported critical dimension of 20 nm<sup>[10,13]</sup> in which magnetic interference between  $\text{Fe}_3\text{O}_4$  to MnO becomes insignificant. In stark contrast, the engineered single composite  $\text{Fe}_3\text{O}_4(8)@\text{MnO}/\text{mSiO}_2$  particle confines all MnO clusters within the “nano volume of magnetic field interference”. Since the magnetization is expressed per magnetic ion per gram, the change of magnetic moment is independent of silica content. As shown in Figure 3d, the anti-parallel spin-spin interaction between the  $\text{Fe}_3\text{O}_4$  NP and MnO clusters within this single nanosize particle causes a large reduction (only one third remains) in the overall magnetic moment of the composite within the “nano influence zone”. However, the physical mixture does not show the significant modulation in overall magnetic moment. From the literature,<sup>[10,13]</sup> it has been emphasized that the magnetic field generated by a super-paramagnetic nanoparticle can subtly perturb the relaxation process of surrounding  $T_1$  CAs (Scheme 1a) because of the strong magnetic coupling and high susceptibility effect of  $T_1$  CA, which induces an undesirable decrease of the  $T_1$ -weighted MR signal. However, the significance of the simultaneous reduction in overall magnetization of CAs as presently observed, which allows fine tuning of magnetic response of the composite particle to external field for magnetic applications, might have been overlooked.



**SCHEMES 1.** The magnetic field generated by a DMCA with different size of core  $\text{Fe}_3\text{O}_4$ . (a) The local  $\Delta B$  generated by  $\text{Fe}_3\text{O}_4$  is greatly reduced by the introduction of MnO NPs within nano influence zone in a single particle. (b) The modulation of magnetic field and imaging property ( $T_1$  or  $T_2$  or dual mode) by tuning the size of  $\text{Fe}_3\text{O}_4$  in a  $\text{Fe}_3\text{O}_4@\text{MnO}/\text{mSiO}_2$ .

**Magnetic field tuning within “nano influence zone”.** According to our observation, the incorporation of



antiferromagnetic MnO clusters in the mesoporous shell appears to greatly modulate the local magnetic field generated by the  $\text{Fe}_3\text{O}_4$  core and thus reduce the net saturation magnetization. This tunable feature of single nanoparticle engineering dependent on size, composition and location of magnetic moieties not only tailors its longitudinal relaxation but also makes the particle become responsive to the external magnetic field strength. To further demonstrate this, we tuned the induced magnetic field by using different sized core  $\text{Fe}_3\text{O}_4$  NPs (3.7 and 17.5 nm) for the preparation of  $\text{Fe}_3\text{O}_4(3.7)@\text{MnO}/\text{mSiO}_2$  and  $\text{Fe}_3\text{O}_4(17.5)@\text{MnO}/\text{mSiO}_2$ . The corresponding TEM images of these particles are shown in Figure S14. It is noted that the thickness of the silica shell of  $\text{Fe}_3\text{O}_4(x)@\text{MnO}/\text{mSiO}_2$  nanocomposites ( $x = 3.7, 8$  and  $17.5$ ) were well-controlled at around 20 nm (can also be a variable to be investigated) and we assumed the dispersion/density of MnO NPs in mesopores is similar among all samples since they were prepared by the same protocol. Table S2 shows the  $[\text{Fe}]$  to  $[\text{Mn}]$  ratio of three  $\text{Fe}_3\text{O}_4@\text{MnO}/\text{mSiO}_2$  nanocomposites. Magnetic properties such as SQUID M-H curves (Figure S15) and relaxation properties (Table S1) of  $\text{Fe}_3\text{O}_4(3.7)@\text{MnO}/\text{mSiO}_2$  and  $\text{Fe}_3\text{O}_4(17.5)@\text{MnO}/\text{mSiO}_2$  were also measured for systematic comparison with  $\text{Fe}_3\text{O}_4(8)@\text{MnO}/\text{mSiO}_2$ . Among these three nanocomposites,  $\text{Fe}_3\text{O}_4(17.5)@\text{MnO}/\text{mSiO}_2$  with the largest iron oxide core exhibits typical  $T_2$  character that possesses highest  $M_s$ ,  $r_2$  and  $r_2/r_1$  ratio. While for  $\text{Fe}_3\text{O}_4(3.7)@\text{MnO}/\text{mSiO}_2$ , the gradual increase of magnetization with external magnetic field and the low  $r_2/r_1$  ratio (13.27), close to  $T_1$  CA  $\text{MnO}/\text{mSiO}_2$  (10.17), both indicate this nanocomposite is much like a  $T_1$  CA. The MR phantom images of  $\text{Fe}_3\text{O}_4(17.5)@\text{MnO}/\text{mSiO}_2$  are shown in Figure S16.  $\text{Fe}_3\text{O}_4@\text{MnO}/\text{mSiO}_2$  was found to lose  $T_1$ -weighted MR imaging capability when the diameter of core  $\text{Fe}_3\text{O}_4$  was increased from 8 nm to 17.5 nm. No apparent influence of embedded MnO clusters on  $T_2$ -weighted MR imaging of  $\text{Fe}_3\text{O}_4(17.5)@\text{MnO}/\text{mSiO}_2$  was observed (c.f.  $\text{Fe}_3\text{O}_4(17.5)@\text{SiO}_2$ , Figure S16 left). It was noted that the strength of the induced magnetic field is proportional to the magnetization of  $\text{Fe}_3\text{O}_4$  while inversely proportional to distance ( $1/r^2$ ) from the center  $\text{Fe}_3\text{O}_4$ . This result indicates the strength of the induced magnetic field of  $\text{Fe}_3\text{O}_4(17.5)@\text{MnO}/\text{mSiO}_2$  within the “nano influence zone” ( $\sim 20$  nm) can efficiently suppress the  $T_1$  signal and the induced magnetic field outside the particle is strong enough to generate a comparable local field inhomogeneity for the  $T_2$  signal (Scheme 1b, right). This suppression of  $T_1$  imaging contrast has been a well-known phenomenon “magnetic quenching effect” when  $T_1$  and  $T_2$  materials are in a close proximity. Surprisingly, the  $\text{Fe}_3\text{O}_4@\text{MnO}/\text{mSiO}_2$  totally lost  $T_2$ -weighted MR imaging capability and became a  $T_1$  CA when the diameter of core  $\text{Fe}_3\text{O}_4$  decreased from 8 nm to 3.7 nm (Figure S17a). It should be noted that  $\text{Fe}_3\text{O}_4(3.7)@\text{SiO}_2$  without MnO clusters clearly exhibits  $T_2$  character. This “inverted MR phenomenon” of contrast agent is observed for the first time presumably due to the intrinsic low magnetization of  $\text{Fe}_3\text{O}_4(3.7)@\text{MnO}/\text{mSiO}_2$  (Figure S15), that the induced magnetic field outside the particle is too weak to generate

local field inhomogeneity (Scheme 1b, left). To further demonstrate our observation,  $\text{Fe}_3\text{O}_4(3.7)@\text{SiO}_2$  and  $\text{MnO}/\text{mSiO}_2$  solution were physically mixed as a function of individual volume percentage from 30% (70%), 50% (50%) to 70% (30%). As shown in Figure S17b, both  $\text{Fe}_3\text{O}_4(3.7)@\text{SiO}_2$  and  $\text{MnO}/\text{mSiO}_2$  retained their original  $T_2$  and  $T_1$  property with signal intensity variation corresponding to volume percentage in the mixed solution. Therefore, the suppression of  $T_2$  signal by incorporating  $T_1$  CAs can also be achieved by tuning the induced magnetic field of  $T_2$  CA within the single nanoparticle as illustrated in Scheme 1b. As  $\text{Fe}_3\text{O}_4(3.7)@\text{MnO}/\text{mSiO}_2$  only exhibits  $T_1$  contrast and  $\text{Fe}_3\text{O}_4(17.5)@\text{MnO}/\text{mSiO}_2$  possessing higher magnetization ( $\sim 2$  emu/g) than  $\text{Fe}_3\text{O}_4(8)@\text{SiO}_2$  ( $\sim 1.5$  emu/g) is also expected to cause damage to the tagged host during MR scanning,  $\text{Fe}_3\text{O}_4(8)@\text{MnO}/\text{mSiO}_2$  with controlled magnetization is thus the best candidate for the safe dual-imaging under MR magnetic field.

By careful examination of the optimal distribution of labelled cells on the ependymal linings of SVZ using this new DMCA, there appears to be non-uniform range from ultrathin to thicker layers, as identified by both MRI modes (Figure S18). On average,  $0.195 \pm 0.020$  mm thickness layers deep down into the delicate ependymal linings under the  $T_1$ -weighted mode and  $0.320 \pm 0.045$  mm linings under the  $T_2$ -weighted mode are observed. Occasionally, an ultrathin white outer lining of 0.02 mm on the ependymal linings can be observed in the  $T_1$ -weighted image. This thickness matches with the reported ependymal linings in specific regions approaching 1 to 2 cell thicknesses (0.015 - 0.050 mm).<sup>[23]</sup> Thus, the fine-tuning of DMCA can improve the image resolution of MRI by reducing their extensive magnetic interference between individual magnetic components. Unsurprisingly, with the sole  $T_1$  CA and  $T_2$  CA with no fine control, we could only see much thicker labelled regions on the ependymal layers with an average thickness of  $0.320 \pm 0.046$  mm and  $0.573 \pm 0.074$  mm, respectively.

## CONCLUSION

We have demonstrated the concept of spatial arrangement of  $T_1$  and  $T_2$  components in a single core-shell nanoparticle as a new DMCA. It can provide optimal higher resolution  $T_1/T_2$  in-vivo imaging of living ependymal brain cells of rodents with no local damage under a strong MRI magnetic field. It is believed that this capability can offer a step towards rational engineering of functional DMCA NPs for a wide range of accurate magnetic manipulations in a safe manner.

## ASSOCIATED CONTENT

**Supporting Information.** Detailed characterization of all nanocomposites and corresponding MR experiments carried out for magnetic field tuning. This material is available free of charge via the Internet at <http://pubs.acs.org>.

## AUTHOR INFORMATION

Corresponding Author

[edman.tsang@chem.ox.ac.uk](mailto:edman.tsang@chem.ox.ac.uk)

## Author Contributions

<sup>†</sup>These authors contributed equally.

## ACKNOWLEDGMENT

YKP and CNPL contributed equally to this work. YKP and SCET are grateful to HKPU for the academic visiting scheme to partial support this work. YKP acknowledges the University of Oxford Clarendon Fund Scholarship for his DPhil study. We are also indebted to the support from Taiwan Mouse Clinic which is currently funded through the National Research Program for Biopharmaceuticals (NRPB) at the Ministry of Science and Technology of Taiwan, particularly for the MRI mouse experiments presented in this paper.

## REFERENCES

- (1) Laurent, S.; Forge, D.; Port, M.; Roch, A.; Robic, C.; Elst, L. V.; Muller, R. N. Magnetic Iron Oxide Nanoparticles: Synthesis, Stabilization, Vectorization, Physicochemical Characterizations, and Biological Applications. *Chem. Rev.* **2008**, *108*, 2064–2110.
- (2) Plouffe, B. D.; Murthy, S. K.; Lewis, L. H. Fundamentals and application of magnetic particles in cell isolation and enrichment: a review. *Rep Prog Phys.* **2015**, *78*, 016601.
- (3) Jun, Y. W.; Lee, J. H.; Cheon, J. Chemical design of nanoparticle probes for high-performance magnetic resonance imaging. *Angew. Chem. Int. Ed.* **2008**, *47*, 5122–5135.
- (4) Kim, J.; Piao, Y.; Hyeon, T. Multifunctional nanostructured materials for multimodal imaging, and simultaneous imaging and therapy. *Chem. Soc. Rev.* **2009**, *38*, 372–390.
- (5) Hu, F.; Zhao, Y. S. Inorganic nanoparticle-based T<sub>1</sub> and T<sub>1</sub>/T<sub>2</sub> magnetic resonance contrast probes. *Nanoscale* **2012**, *4*, 6235–6243.
- (6) Peng, Y.-K.; Lai, C.-W.; Liu, C.-L.; Chen, H.-C.; Hsiao, Y.-H.; Liu, W.-L.; Tang, K.-C.; Chi, Y.; Hsiao, J.-K.; Lim, K.-E.; Liao, H.-E. Shyue, J.-J.; Chou, P.-T. A New and Facile Method To Prepare Uniform Hollow MnO/Functionalized mSiO<sub>2</sub> Core/Shell Nanocomposites. *ACS Nano*, **2011**, *5*, 4177–4187.
- (7) Peng, Y.-K.; Lai, C.-W.; Hsiao, Y.-H.; Tang, K.-C.; Chou, P.-T. Multifunctional Mesoporous Silica-Coated Hollow Manganese Oxide Nanoparticles for Targeted Optical Imaging, T<sub>1</sub> Magnetic Resonance Imaging and Photodynamic Therapy. *Mater. Express* **2011**, *1*, 136–143.
- (8) Peng, Y.-K.; Tsang, S. C. E.; Chou, P.-T. Chemical design of nanoprobe for T<sub>1</sub>-weighted magnetic resonance imaging. *Mater. Today*. **2016**, *19*, 336–348.
- (9) Bae, K. H.; Kim, Y. B.; Lee, Y.; Hwang, J.; Park, H.; Park, T. G. Bioinspired Synthesis and Characterization of Gadolinium-Labeled Magnetite Nanoparticles for Dual Contrast T<sub>1</sub>- and T<sub>2</sub>-Weighted Magnetic Resonance Imaging. *Bioconjugate Chem.* **2010**, *21*, 505–512.
- (10) Choi, J. S.; Lee, J. H.; Shin, T. H.; Song, H. T.; Kim, E. Y.; Cheon, J. Self-Confirming “AND” Logic Nanoparticles for Fault-Free MRI. *J. Am. Chem. Soc.* **2010**, *132*, 11015–11017.
- (11) Yanga, H.; Zhuanga, Y.; Sund, Y.; Daia, A.; Shib, X.; Wue, D.; Lid, F.; Hua, H.; Yanga, S. Targeted dual-contrast T<sub>1</sub>- and T<sub>2</sub>-weighted magnetic resonance imaging of tumors using multifunctional gadolinium-labeled superparamagnetic iron oxide nanoparticles. *Biomaterials* **2011**, *32*, 4584–4593.
- (12) Im, G. H.; Kim, S. M.; Lee, D.-G.; Lee, W. J.; Lee, J. H.; Lee, I. S. Fe<sub>3</sub>O<sub>4</sub>/MnO hybrid nanocrystals as a dual contrast agent for both T<sub>1</sub>- and T<sub>2</sub>-weighted liver MRI. *Biomaterials* **2013**, *34*, 2069–2076.
- (13) Shin, T.-H.; Choi, J.-S.; Yun, S.; Kim, I.-S.; Song, T.-H.; Kim, Y.; Park, I. K.; Cheon, J. T<sub>1</sub> and T<sub>2</sub> Dual-Mode MRI Contrast Agent for Enhancing Accuracy by Engineered Nanomaterials. *ACS Nano* **2014**, *8*, 3393–3401.
- (14) Li, S.; Shao, C.; Gu, W.; Wang, R.; Zhang, J.; Lai, J.; Li, H.; Ye, L. Targeted imaging of brain gliomas using multifunctional Fe<sub>3</sub>O<sub>4</sub>/MnO nanoparticles. *RSC Adv.* **2015**, *5*, 33639–33645.
- (15) Wang, X.; Niu, D.; Wu, Q.; Bao, S.; Su, T.; Liu, X.; Zhang, S.; Wang, Q. Iron oxide/manganese oxide co-loaded hybrid nanogels as pH-responsive magnetic resonance contrast agents. *Biomaterials* **2015**, *53*, 349–357.
- (16) Kim, B. H.; Lee, N.; Kim, H.; An, K.; Park, Y. I.; Choi, Y.; Shin, K.; Lee, Y.; Kwon, S. G.; Na, H. B.; Park, J.-G.; Ahn, T.-Y.; Kim, Y.-W.; Moon, W. K.; Choi, S. H.; Hyeon, T. Large-Scale Synthesis of Uniform and Extremely Small-Sized Iron Oxide Nanoparticles for High-Resolution T<sub>1</sub> Magnetic Resonance Imaging Contrast Agents. *J. Am. Chem. Soc.* **2011**, *133*, 12624–12631.
- (17) Niu, D.; Luo, X.; Li, Y.; Liu, X.; Wang, X.; Shi, J. Manganese-Loaded Dual-Mesoporous Silica Spheres for Efficient T<sub>1</sub>- and T<sub>2</sub>-Weighted Dual Mode Magnetic Resonance Imaging. *ACS Appl. Mater. Interfaces* **2013**, *5*, 9942–9948.
- (18) Lui, C. N. P.; Tsui, Y. P.; Ho, A. S. L.; Shum, D. K. Y.; Chan, Y. S.; Wu, C. T.; Li, H. W.; Tsang, S. C. E.; Yung, K. K. L. Neural Stem Cells Harvested from Live Brains by Antibody-Conjugated Magnetic Nanoparticles. *Angew. Chem. Int. Ed.* **2013**, *52*, 12298–12302.
- (19) Peng, Y.-K.; Lui, C. N. P.; Lin, T.-H.; Chang, C.; Chou, P.-T.; Yung, K. K. L.; Tsang, S. C. E. Multifunctional silica-coated iron oxide nanoparticles: a facile four-in-one system for in situ study of neural stem cell harvesting. *Faraday Discuss.* **2014**, *175*, 13–26.
- (20) Baek, M. J.; Park, J. Y.; Xu, W.; Kattel, K.; Kim, H. G.; Lee, E. J.; Patel, A. K.; Lee, J. J.; Chang, Y.; Kim, T. J.; Bae, J. E.; Chae, K. S.; Lee, G. H. Water-Soluble MnO Nanocolloid for a Molecular T<sub>1</sub> MR Imaging: A Facile One-Pot Synthesis, In vivo T<sub>1</sub> MR Images, and Account for Relaxivities. *ACS Appl. Mater. Inter.* **2010**, *2*, 2949–2955.
- (21) Peng, Y.-K.; Liu, C.-L.; Chen, H.-C.; Chou, S.-W.; Tseng, W.-H.; Tseng, Y.-J.; Kang, C.-C.; Hsiao, J.-K.; Chou, P.-T. Antiferromagnetic Iron Nanocolloids: A New Generation in Vivo T<sub>1</sub> MRI Contrast Agent. *J. Am. Chem. Soc.* **2013**, *135*, 18621–18628.
- (22) Peng, Y.-K.; Tseng, Y.-J.; Liu, C.-L.; Chou, S.-W.; Chen, Y.-W.; Tsang, S. C. E.; Chou, P.-T. One-step synthesis of degradable T<sub>1</sub>-FeOOH functionalized hollow mesoporous silica nanocomposites from mesoporous silica spheres. *Nanoscale* **2015**, *7*, 2676–2687.
- (23) Kim, J. B.; Greber, B.; Araúz-Bravo, M. J.; Meyer, J.; Park, K. I.; Zaehres, H.; Schöler, H. R. Direct reprogramming of human neural stem cells by OCT4. *Nature* **2009**, *461*, 649–653.

